Coalescence-induced droplet jumping on superhydrophobic surfaces: Effects of droplet mismatch

Joram Wasserfall, Patric Figueiredo, Reinhold Kneer, Wilko Rohlfs,* and Philipp Pischke
Institute of Heat and Mass Transfer, RWTH Aachen University, Augustinerbach 6, 52056 Aachen, Germany
(Received 19 January 2017; published 4 December 2017)

On low-adhesion surfaces, coalescing droplets can spontaneously jump off, known as coalescence-induced droplet jumping. It is observed on a variety of synthetic and natural superhydrophobic surfaces, and gives rise to a range of applications, such as self-cleaning condensers, anti-icing coatings, and thermal diodes. Through three-dimensional simulations, this paper demonstrates the fluid dynamics of droplet jumping upon binary unequal-sized-droplet coalescence. Parametric studies show the influence of droplet mismatch, viscosity, and contact angle on jumping velocities, where liftoff regimes are defined on the basis of Ohnesorge number and droplet size ratio. Because of the strong asymmetric flow behavior, the well-known small conversion efficiency for equal-sized-droplet jumping, where around 6% of the released surface energy is convertible into translational kinetic energy, is further reduced for unequal-sized-droplet jumping. The findings offer insights into their fluid dynamics and give a starting point for further modeling of dropwise condensation on superhydrophobic surfaces.

DOI: 10.1103/PhysRevFluids.2.123601

I. INTRODUCTION

On low-adhesion surfaces, droplet coalescence can induce a translational motion directed away from the solid surface [1,2]. Such coalescence-induced droplet jumping was first recorded during experiments with condensed mercury drops by Kollera and Grigull in 1969 [1]. Recently, droplet jumping has attracted renewed attention in the context of material sciences and the development of synthetic and natural superhydrophobic surfaces [2–4].

Figure 1 illustrates the different stages of droplet jumping. At the onset of coalescence, droplets form a capillary bridge, which extends due to capillary forces and results in an oscillatory motion [5]. The solid surface breaks the axisymmetric motion, accelerating the merged droplet away from the solid surface. Depending on the ratio of surface energy to viscous dissipation, the upward motion may cause droplets to detach from the solid surface. This self-propelled mechanism can remove droplets with diameters much smaller than the capillary length, enhancing efficiency in a range of applications, such as condensers [6,7], self-cleaning surfaces [8,9], anti-icing coatings [10,11], and thermal diodes [12]. In addition, jumping droplets may gain a net positive charge [13], which can be used for energy harvesting [14] or for electric-field-enhanced droplet jumping [15,16].

The fluid dynamics of droplet coalescence on solid surfaces is governed by a balance of surface energy, kinetic energy, and viscous dissipation, neglecting gravitational effects. During coalescence, the overall droplet surface area is reduced and surface energy is released. On low-adhesion surfaces and for vanishing viscous forces, the excess energy may propel the merged droplet away from the solid surface. The energy balance for the fundamental case with two inviscid spherical droplets with different radii R_1 and R_2 on a surface with no adhesion gives a characteristic jumping velocity,

$$U = \sqrt{\frac{\sigma}{\rho_l R_1}\frac{f(k)}{f(1)}}, \tag{1}$$

*rohlfs@wsa.rwth-aachen.de

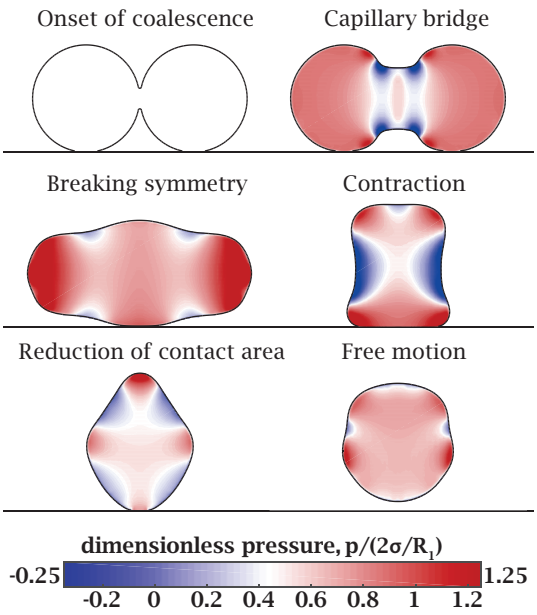

FIG. 1. Mechanism of coalescence-induced droplet jumping. The coalescence of droplets leads to the release of surface energy, which is converted into translational motion. The static pressure field is scaled with the capillary pressure.

where σ is the surface tension and ρ_l is the density of the liquid droplets [2]. The function $f(k)$ is a geometry parameter describing the effect of droplet mismatch,

$$f(k) = \frac{1 + k^2 - (1 + k^3)^{2/3}}{1 + k^3}, \tag{2}$$

with the droplet size ratio

$$k = \frac{R_2}{R_1}, \tag{3}$$

where R_2 is the radius of the smaller droplet. For $R_1 = R_2 = R$ and $k = 1$, this definition simplifies to $U = [\sigma/(\rho_l R)]^{1/2}$, which is consistent with the terminology in literature used for equal-sized-droplet jumping [2,17,18]. Unsteady motion is governed by the capillary-inertial time scale of coalescence [19,20]:

$$\tau = \sqrt{\frac{\rho_l R_1^3}{\sigma}} \tag{4}$$

By introducing capillary-inertial scaling from Eqs. (1) and (4), coalescence-induced droplet jumping can be characterized in terms of dimensionless time scales $t^* = t/\tau$ and velocities $u^* = u/U$. Similarly, the influence of viscous damping and gravity is given by appropriate dimensionless numbers, i.e., Ohnesorge number

$$\mathrm{Oh} = \frac{\mu}{\sqrt{R_1 \rho_l \sigma}} \tag{5}$$

and Bond number $\mathrm{Bo} = (\rho_l g R_1^2)/\sigma$, where μ is the dynamic viscosity of the droplet and g is the gravitational acceleration. In this study, the influence of gravity is neglected ($\mathrm{Bo} = 0$). Finally,

wall adhesion is described on the basis of contact angle θ, which is a dimensionless quantity of its own.

In condensation experiments on superhydrophobic surfaces, coalescence of microdroplets with diameters between 10 and 300 μm has induced jumping velocities below the characteristic velocity, ranging from $u^* = 0.18$ to $u^* = 0.24$ [2,18]. Similar droplet jumping velocities with $u^* = 0.21$ were measured on a heated substrate, exploiting the Leidenfrost effect to achieve nonwetting conditions [21]. Despite larger Ohnesorge numbers, nanodroplet coalescence with diameters around 0.6 μm can also induce droplet jumping [22,23]. Because of the small scale of the phenomenon, experimental studies cannot reveal the wetting state, which strongly influences the jumping velocity [24]. In addition to experimental studies, numerical investigations reveal insights into the jumping mechanism of equal-sized-droplet coalescence, as illustrated in Fig. 1 [17,25]. Liu *et al.* divide the jumping process into four stages [17]: In stage I, the capillary bridge between the droplets extends as in the case of droplet coalescence in free flow. The axisymmetric motion is broken as the capillary bridge reaches the wall, initiating stage II. In this stage, the solid surface forces the droplet into an upward motion, which is maintained by the contraction of the merged drop. In stage III, the upward motion leads to a reduction of contact area, while the droplet decelerates. If viscous dissipation and adhesive forces dominate over inertia, the droplet loses its kinetic energy and adheres to the surface; otherwise, the droplet detaches and jumps off the surface, initiating a free motion in the gas phase, stage IV. Note that at the time of detachment the kinetic energy consists of an oscillatory part and a translational part [17]. Recently, Enright *et al.* derived a semiempirical model based on energy conservation, demonstrating that the jumping velocity toward the inviscid limit is approximately $u^* = 0.28$ [18]. Consequently, coalescence-induced droplet jumping is fundamentally ineffective, as only 6% of the released surface energy is converted into translational kinetic energy. As viscous forces damp coalescence, no jumping is observed for droplets with Ohnesorge numbers above $\mathrm{Oh} > 0.4$ on ideal, nonwetting surfaces [17]. Likewise, adhesive forces limit the jumping phenomenon to wetting conditions with contact angles of $\theta > 150^\circ$ [26,27].

Previous studies focused on jumping induced by coalescence of equal-sized droplets only, whereas this study examines droplet jumping upon binary unequal-sized-droplet coalescence using three-dimensional fully resolved numerical simulations. In Sec. II A, a theoretical energy balance is presented that introduces an absolute criterion for droplet jumping of unequal-sized droplets. In Sec. III, the applied numerical methodology is described. The results in Sec. IV are subdivided into three subsections. Section IV A illustrates the fluid motion for an exemplary case of unequal-size droplet jumping. Section IV B provides data for the jumping velocity and the jumping angle depending on droplet size ratio, Ohnesorge number, and contact angle. Finally, Sec. IV C discusses the transition from the regime of adhering to jumping based on energy balances. In Sec. V, our conclusion is presented.

II. STATIC ENERGY BALANCES

A fundamental balance of surface energies during the process of droplet coalescence and droplet jumping allows us to identify a hard condition under which droplet jumping can occur. For this, the surface and adhesion energy of three different static states as shown in Fig. 2 are considered. In state 1, two sessile droplets are attached to the surface with a given contact angle. In state 2, a stationary merged droplet appears and, finally in state 3, a detached droplet. The total liquid volume is equal in all three cases.

During coalescence, the change in surface energy is described by

$$\Delta E_{\mathrm{s,merge}} = \sigma[\Delta A_{\mathrm{lg}} - \Delta A_{\mathrm{ls}}\cos(\theta)], \tag{6}$$

where ΔA_{lg} is the change in area between liquid (l) and gas (g) phases and ΔA_{ls} is the change in contact area between liquid and solid (s) phases. This yields

$$\Delta E_{\mathrm{s,merge}} = \sigma[A_{\mathrm{D},1} + A_{\mathrm{D},2} - A_{\mathrm{D},1+2} - (A_{\mathrm{C},1} + A_{\mathrm{C},2} - A_{\mathrm{C},1+2})\cos(\theta)], \tag{7}$$

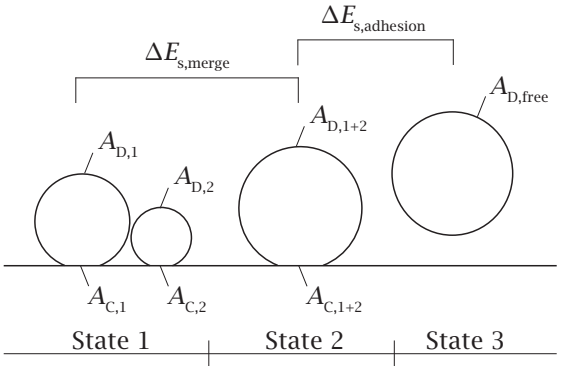

FIG. 2. Surface and adhesion energy of three different static states.

with

$$A_{D,i}(r,\theta) = \pi r^2[(1-(\cos\theta)^2)+(1-\cos\theta)^2] \tag{8}$$

and

$$A_{C,i}(r,\theta) = \pi r^2[1-\cos^2\theta]. \tag{9}$$

The excess in surface energy is released, leading to a droplet motion (kinetic energy) and to an oscillation with droplet deformation (energy stored in surface energy).

Detaching the joint sessile drop from the surface results in an increase in surface area and thus requires energy. The energy difference between the sessile drop and the free drop is as such given by

$$\Delta E_{s,adhesion} = \sigma[A_{D,sessile} - A_{D,free} - A_{C,sessile}\cos(\theta)], \tag{10}$$

where the surface area of the sessile droplet and the contact area are equal to $A_{D,1+2}$ and $A_{C,1+2}$, respectively.

An absolute criterion for droplet jumping is given by $\Delta E_{s,merge} > \Delta E_{s,adhesion}$. Figure 3 (left) illustrates the ratio between the energy of droplet merging and the adhesion energy of droplet detachment. For large differences in droplet size (small values of k), $\Delta E_{s,merge}$ is not sufficient for droplet jumping. The contact angle significantly influences the energy for droplet detachment.

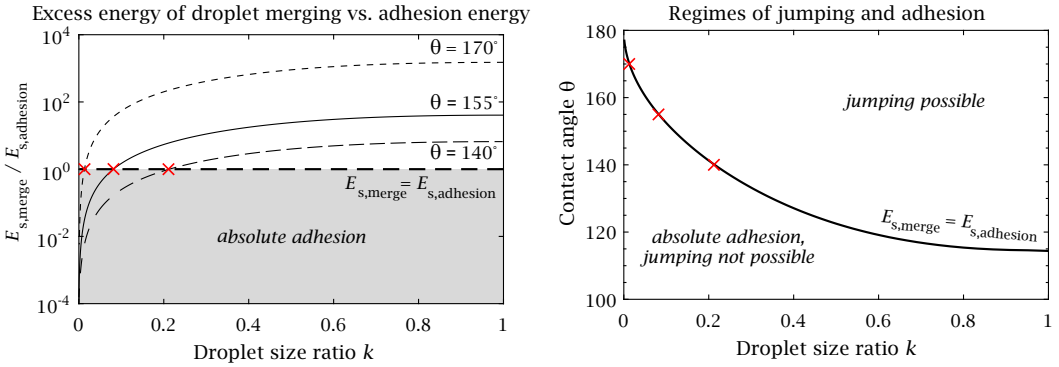

FIG. 3. Ratio between the excess energy of droplet merging and the adherence energy depending on droplet size ratio and contact angle (left). Regime diagram for the absolute jumping limit (right). Coinciding values are marked by the red crosses.

Figure 3 (right) shows the absolute border of adhesion depending on droplet ratio and contact angle. For low values of k, the contact angle regime in which jumping is still possible approaches 180°. For equal-size droplets, the minimum contact angle for droplet jumping is $\theta = 114.4°$. Beyond this contact angle, the energy released by the merging droplet is smaller than the energy of droplet detachment, irrespectively the droplet ratio. Note that this energy balance assumes that the entire energy of droplet merging is available to detach the droplet from the surface. However, only a small portion is converted into translational energy. A large amount of the released energy results in droplet oscillation, not contributing to droplet detachment, as shown in the next chapter. Furthermore, inviscid flow is assumed, thus neglecting viscous dissipation.

III. METHODS

Coalescence-induced droplet jumping is described by an incompressible two-fluid flow, where the motion is governed by the Navier-Stokes equations. Interfacial forces originate from curvature only. At the three-phase contact line, a constant contact angle is assumed to restrict the number of influencing parameters.

A. Direct numerical simulation technique

The numerical simulation of coalescence-induced droplet jumping is performed with a modified version of the volume-of-fluid (VOF) solver implemented in the open-field operation and manipulation libary (openFOAM; see Jasak [28] and Rusche [29]). The VOF method describes the flow of more than one fluid by cell-averaged volume fractions α [30]. In the conservation equations, fluid properties such as density and viscosity depend on the volume fractions of the liquid and gaseous phase such that $\rho = \alpha\rho_l + (1-\alpha)\rho_g$ and $\mu = \alpha\mu_l + (1-\alpha)\mu_g$. The continuity and momentum equations for the two-fluid flow are respectively

$$\frac{\partial \rho}{\partial t} + \nabla(\rho \times \boldsymbol{U}) = 0 \tag{11}$$

and

$$\frac{\partial}{\partial t}(\rho\,\boldsymbol{U}) + \nabla(\rho\,\boldsymbol{U} \otimes \boldsymbol{U}) = \nabla\boldsymbol{\tau} - \nabla p + \boldsymbol{f}. \tag{12}$$

Within the momentum equation, the left hand accounts for inertia effects, while the right side accounts for viscous stresses $\boldsymbol{\tau}$ and pressure p. Interfacial volume forces $\boldsymbol{f}$ are nonzero at the interface and zero elsewhere. Since pressure and density are not coupled by state equations in incompressible flows, the pressure field is obtained implicitly by a projection scheme to ensure mass conservation by splitting of operators (the PISO algorithm).

For the two-fluid flow with constant densities, the volume fraction is a conservative scalar, and its advection by the velocity field $\boldsymbol{U}$ is described by following transport equation:

$$\frac{\partial \alpha}{\partial t} + \nabla(\alpha \otimes \boldsymbol{U}) = 0. \tag{13}$$

As the finite-volume discretization defines cell-average volume fractions, the interface is represented by mixed cells that contain both fluids. To avoid numerical diffusion of the interface, the standard openFOAM VOF-solver interFoam introduces an artificial antidiffusive flux in the direction normal to the interface, known as the interface compression method. In capillary-dominated flows as considered here, interfacial forces must be obtained from the curvature of the interface. If the exact interface location is not required, interface curvature κ can be reconstructed from the divergence of the interface normal vector $\hat{\boldsymbol{n}}$ using vector field calculus

$$\kappa = -\nabla\hat{\boldsymbol{n}}. \tag{14}$$

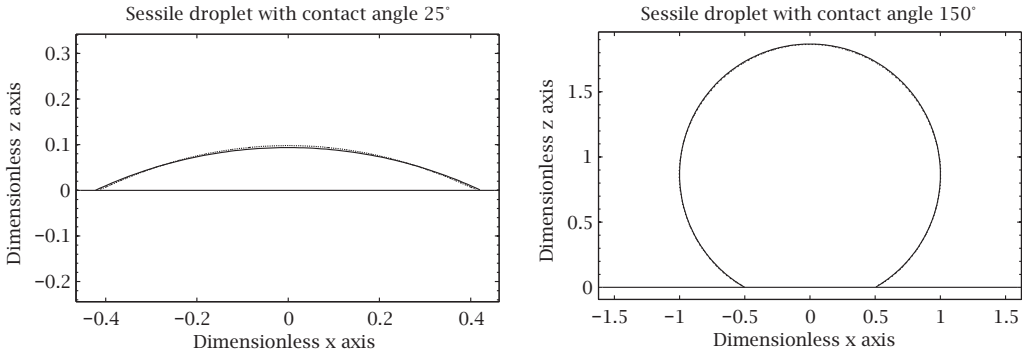

FIG. 4. Shape of sessile drops at two different contact angles: present solver $(\cdots)$ and theory $(-)$. Errors are in the order of $\epsilon \approx 10^{-2}$, measured by the location of the droplet centroid.

The interface orientation $\hat{\boldsymbol{n}}$ is obtained from normalizing the gradient of the volume fraction

$$\hat{\boldsymbol{n}} = \frac{\nabla\alpha}{||\nabla\alpha||}. \tag{15}$$

This method is implemented in the interFoam solver. The resulting interfacial forces are converted into cell-average volume forces by the continuum surface force method. Because of accuracy limitations in interFoam [31], the interface compression scheme was amended by a limiter to avoid artificial oversharpening of the interface [32,33]. Interfacial forces are calculated by the continuum surface stress method [34].

The new variant of interFoam has the following advantages over its original. First, capillary pressures are predicted correctly. Second, predictions do not depend on the strength of the antidiffusive flux. Third, the predictions are independent of the frame of reference, which is not the case with the original interFoam formulation, but crucial to calculations of traveling waves in falling liquid films, which can be considered steady-state problems in a frame of reference moving at phase velocity [33]. A detailed description of the model together with a validation based on various test cases is given in Ref. [32]. Results of a test case showing the shape of a sessile droplet and an oscillating droplet are presented in Figs. 4 and 5 respectively.

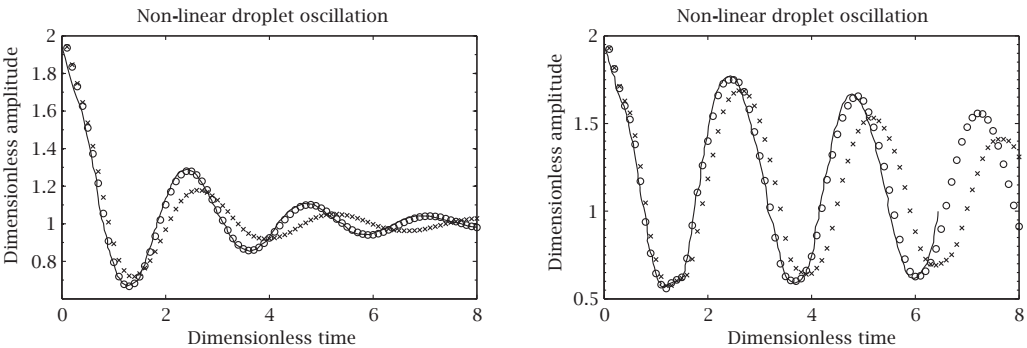

FIG. 5. Nonlinear droplet oscillations: present solver $(\circ)$, interFoam $(\times)$, and numerical reference data from literature [35,36] $(-)$. Dimensionless oscillation for high damping (Re $= 10$, left) and low damping (Re $= 100$, right). Due to the imprecise calculation of capillary pressures, interFoam fails to predict droplet oscillations accurately. The present solver agrees well with reference simulations.

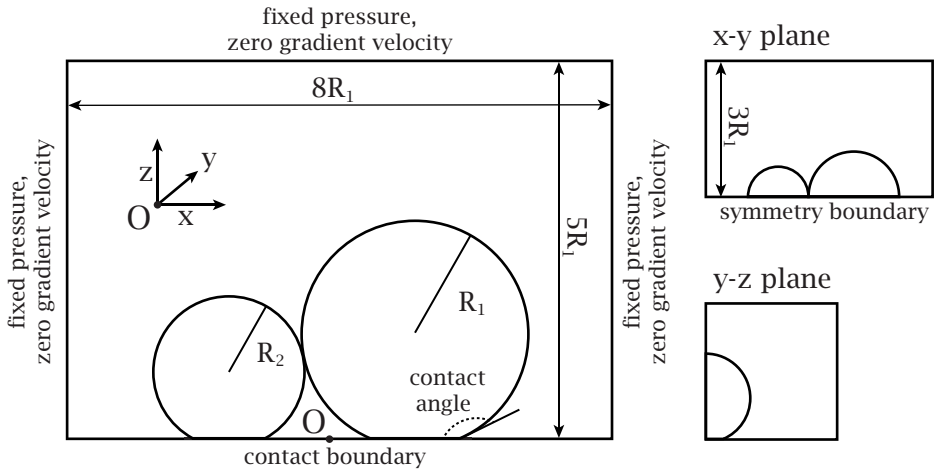

FIG. 6. Simulation case with boundary conditions. The smallest cell size after dynamic mesh refinement is $0.025/R_1$.

B. Contact angle boundary condition

The contact angle boundary condition is of specific importance for the phenomenon of droplet coalescence on a substrate. It prescribes the orientation of the interface at the contact line (substrate-droplet-gas) and requires the correct prediction of adhesion forces. In reality, contact angles also depend on contact line movement such that different dynamic contact angle models exist. Accounting for dynamic contact angles increases the parameter space and thus the complexity of the problem significantly. Thus, this first study on the influence of droplet mismatch on droplet jumping is limited to constant contact angles.

The surface energies of the interfaces between the different phases determine the contact angle that is formed at the wall. The interface orientation at the wall obtained from the advection of the volume fraction α does not obey necessarily this condition. To maintain the wettability condition prescribed by the given contact angle θ, the interface orientation at the wall is corrected in each time step. The uncorrected contact angle θ_u can be calculated from the uncorrected interface normal at the wall $\hat{\boldsymbol{n}}_\mathrm{u}$ and the normal vector of the wall $\hat{\boldsymbol{n}}_\mathrm{w}$ with

$$\hat{\boldsymbol{n}}_\mathrm{u} \cdot \hat{\boldsymbol{n}}_\mathrm{w} = \cos\theta_\mathrm{u}. \tag{16}$$

The uncorrected interface normal vector at the wall $\hat{\boldsymbol{n}}_\mathrm{u}$ is corrected to $\hat{\boldsymbol{n}}_\mathrm{c}$, which is the vector that fulfills the given contact angle boundary condition:

$$\hat{\boldsymbol{n}}_\mathrm{c} \cdot \hat{\boldsymbol{n}}_\mathrm{w} = \cos\theta. \tag{17}$$

An additional constrain is that the vector $\hat{\boldsymbol{n}}_\mathrm{w}$ lies in the plane defined by the current normal vector $\hat{\boldsymbol{n}}_\mathrm{u}$ and the normal vector of the wall $\hat{\boldsymbol{n}}_\mathrm{w}$:

$$\hat{\boldsymbol{n}}_c = a\,\hat{\boldsymbol{n}}_u + b\,\hat{\boldsymbol{n}}_\mathrm{w}. \tag{18}$$

The coefficients a and b can be determined with Eqs. (16) and (17).

C. Initialization

For coalescence-induced droplet jumping, a Cartesian mesh is used for spatial discretization with adaptive mesh refinement near the interface to ensure sufficient resolution without inflating overall computational cost. Time step is controlled dynamically to ensure the stability limits imposed by the Courant number and capillary time scales. The simulation setup is sketched in Fig. 6. Physical

properties and boundary conditions are defined by Ohnesorge number, droplet size ratio, and contact angle. In this study, gravitational forces are neglected (Bond number equal to zero). Owing to the small droplet size in experimentally observed droplet jumping [18], gravitational forces have a minor influence on the droplet shape which is predominantly affected by surface tension. However, gravity plays a major role in jumping height, which is beyond the scope of this study. Density and viscosity ratio between liquid phase (l) and gas phase (g) are constant at $\rho_l/\rho_g = 1000$ and $\mu_l/\mu_g = 60$, which are reasonable approximations for ambient water-air systems. As introduced before, the following results are presented in terms of dimensionless time $t^* = t/\tau$ and velocities $u^* = u/U$.

D. Evaluation

Droplet velocities $\bar{u}^*$ are defined by mass averaging the respective velocity component u^* over the entire liquid volume V_l,

$$\bar{u}^* = \frac{\int_{V_l} \rho_l u^* \, dV}{\int_{V_l} \rho_l \, dV}. \tag{19}$$

Note that the dimensionless jumping velocity $\bar{u}^*_j$ is directly related to the conversion efficiency of coalescence-induced droplet jumping with [2,18]

$$\frac{E_{trans}}{\Delta E_{s,merge,\theta=180^\circ}} \approx \frac{(\bar{u}^*_j)^2}{6\, f(1)}, \tag{20}$$

where E_{trans} is the translational kinetic energy of the droplet and $\Delta E_{s,merge}$ is the theoretically maximum excess surface energy. The kinetic energy of the droplet is calculated by integrating the absolute velocity over the entire liquid volume with

$$E_k = \frac{1}{2}\int_{V_l} \rho_l u^2 \, dV = E_{trans} + E_{osc}, \tag{21}$$

where in the absence of any rotational motion, the kinetic energy consists of a translational part E_{trans} and an oscillatory part E_{osc}.

IV. RESULTS AND DISCUSSION

In the first part of this section, the fundamental fluid dynamics are investigated by presenting time-evolution data of pressure contours and droplet velocities. Subsequently, jumping velocity and jumping angle are discussed with a comparison to experimental data on superhydrophobic surfaces. Finally, a detailed investigation of the transition from adherence to jumping is presented based on energy arguments.

A. Exemplary case of droplet jumping

The fundamental fluid dynamics of coalescence-induced droplet jumping is presented in Fig. 7 for nearly nonwetting and low-viscosity conditions of $Oh = 0.01$, $k = 0.67$, and $\theta = 170^\circ$. Droplets are initialized in their steady-state shapes, with the large droplet on the left (large droplet side [l.d.s.]), and the small droplet on the right (small droplet side [s.d.s.]). The contours show the pressure field with red and blue coloring, giving an intuitive illustration of the acting capillary forces and of traveling capillary waves. In addition to these qualitative data, instantaneous wall-normal (n) and wall-parallel (p) velocities of the coalesced droplet are shown in Fig. 8. Following Figs. 7 and 8, the considered jumping motion can be divided into four stages, similar to binary equal-sized-droplet coalescence [17]. In the first stage (I), the coalescing droplets form a capillary bridge, which extends due to strong curvature and surface forces at the meniscus. For low-Ohnesorge-number regime with $Oh \ll 1$, the bridge flow is dominated by capillary and inertial forces; for droplets with $k > 0.6$, the growth of the bridge radius follows $r_b/R \sim (t/\tau)^{1/2}$ [19,20,37]. As the capillary bridge expands, two capillary

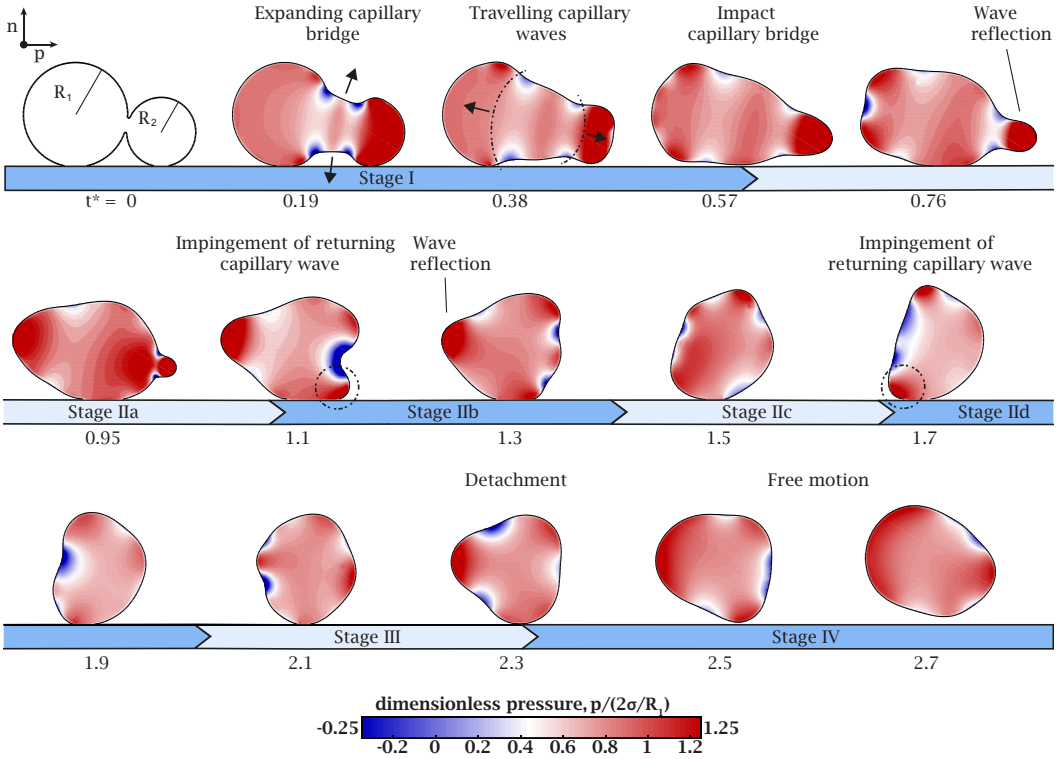

FIG. 7. Time evolution of droplet shape for Oh = 0.01, $k = 0.67$, and $\theta = 170^\circ$. The contours in the symmetry plane show the static pressure (adimensionalized with the capillary pressure). Two acceleration mechanisms are identified: impact of the capillary bridge and impingement of capillary waves. The droplet detaches from the solid surface at $t^* \approx 2.3$, initiating free motion in the gas phase. A movie is provided in the Supplemental Material [38].

waves are induced and travel along the interface away from the bridge region. The waves are characterized by high- and low-pressure regions near the interface, which are noticeable in the pressure contours in Fig. 7 between $t^* = 0.19$ and $t^* = 0.57$. In stage I, low interaction between the merged droplet and the solid surface leads to near-zero wall-normal and wall-parallel velocities; see Fig. 8.

Stage IIa is initiated as the capillary bridge impacts on the solid surface, which forces the droplet into an upward motion. The oblique capillary bridge induces an additional wall-parallel velocity toward the s.d.s., as shown in Fig. 8, which is still by two orders of magnitude smaller than the wall-normal velocity. Thus, the first acceleration mechanism is clearly associated with the expanding bridge flow bounded by the solid surface.

Once the capillary waves reach the sides of the merged droplet, they are reflected on the s.d.s. at $t^* = 0.76$ and on the l.d.s. at $t^* = 1.3$. In stage IIb, the returning capillary wave from the s.d.s. runs into the solid surface, which is the second acceleration mechanism, observable at $t^* = 1.1$. The impinging wave is associated with strong curvatures and high pressures near the three-phase contact line as shown in Fig. 7, which induces further acceleration in the wall-normal direction, as given in Fig. 8. In stage IIc, both acceleration mechanisms (expanding bridge and impinging wave) come to a stop, as shown in a short disruption in wall-normal velocity in Fig. 8. Finally, in stage IId, the returning capillary wave from the l.d.s. runs into the solid surface, as seen at $t^* = 1.7$, causing a similar acceleration mechanism as in stage IIb.

A maximum wall-normal velocity with $\bar{u}^* = 0.18$ is reached at $t^* = 2$, initiating stage III. From this stage, the droplet behaves similarly to a single droplet after an initial disturbance; i.e., it is

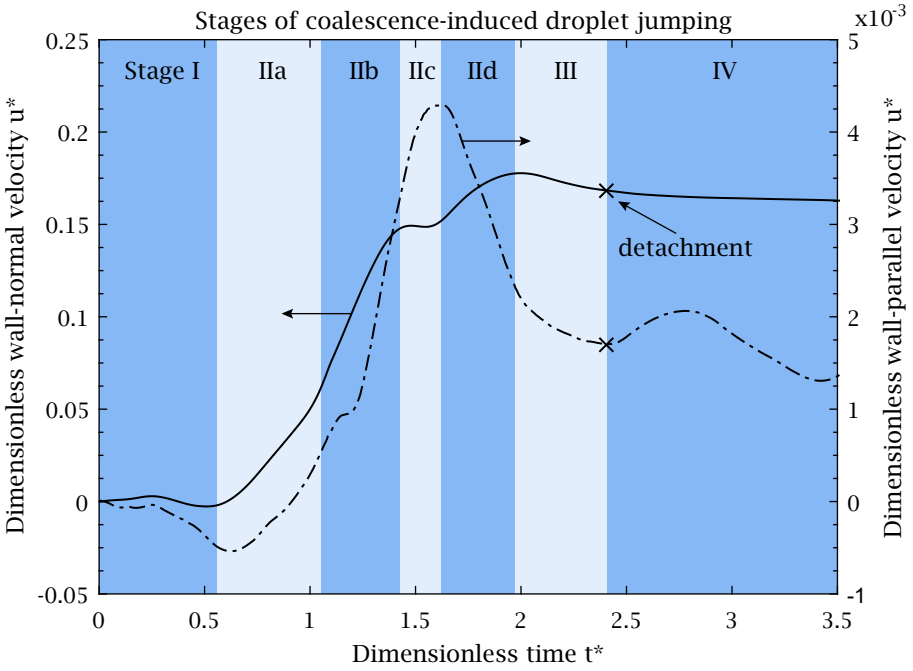

FIG. 8. Time evolution of droplet wall-normal (—left axis) and wall-parallel (- - - right axis) velocity for Oh $= 0.01$, $k = 0.67$, and $\theta = 170°$. Coalescence-induced droplet jumping can be divided into four stages: expansion of the capillary bridge (I), acceleration off the surface (II), deceleration (III), and free motion (IV). Stage II can be divided into substages based on dominating acceleration mechanisms: impact of capillary bridge (IIa), impingement of capillary wave on s.d.s. (IIb), no acceleration (IIc), and impingement of capillary wave on l.d.s. (IId).

stabilized by wall adhesion, leading to a decreasing wall-normal velocity as given in Fig. 8. If the initial momentum at the beginning of stage III dominates over wall adhesion, the droplet will detach. In the given case, detachment occurs at $t^* \approx 2.3$, initiating free motion in stage IV with nearly constant deceleration in the surrounding gas phase. At the time of detachment, the wall-parallel velocity is by two orders of magnitude smaller than the wall-normal velocity, resulting in a jumping direction approximately perpendicular to the surface, with a wall-normal velocity of $\bar{u}^* = 0.17$.

The timings of stages I and II substantially depend on droplet size ratio. For further investigation, the time evolution of the wall-normal velocity for droplet size ratios $k = 1$, $k = 0.67$, and $k = 0.5$ is shown in Fig. 9.

In stage I, the expanding capillary bridge travels shorter distances for larger droplet mismatches before reaching the solid surface; consequently, the onset of upward motion as caused by the impacting capillary bridge occurs earlier for larger droplet mismatches.

In stages IIb–IId, droplet wall-normal acceleration is dominated by traveling capillary waves, as discussed before. For equal-sized droplets, capillary waves travel synchronously and both reflections impinge the solid surface simultaneously in stage IId, while stages IIb and IIc do not exist. For the unequal-sized-droplet coalescence, capillary waves travel asynchronously on the s.d.s. and l.d.s., and the impingement of the reflected waves on the solid surface is offset: First the wave on the s.d.s runs into the solid surface in stage IIb; afterward the wave on the l.d.s runs into the solid surface in stage IId, as discussed earlier. These stages are linked by stage IIc, where there is no droplet acceleration. Because of reduced travel time, the impact of the capillary wave on the s.d.s in stage IIb occurs earlier for larger droplet mismatches. Here, all dimensionless scales refer to the large droplet radius,

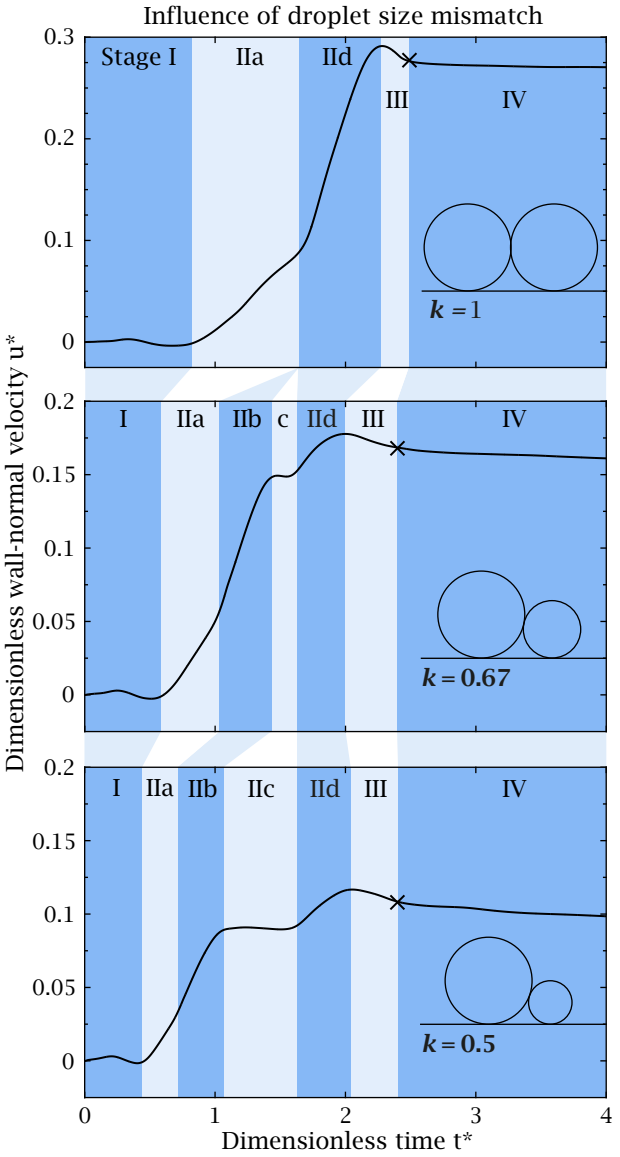

FIG. 9. Time evolution of droplet wall-normal velocity for Oh = 0.01 and $\theta = 170^\circ$, with droplet size ratios of $k = 1$, $k = 0.67$, and $k = 0.5$. The scaling of the velocity axis is not uniform. As the travel times of the capillary bridge and the capillary waves depend on droplet geometries, the stages of coalescence-induced droplet jumping are shifted by droplet size ratio. Detachment and jumping velocity $\bar{u}_j^*$ is defined by zero contact area (×).

the impact of the capillary wave on the l.d.s. in stage IId does not change significantly with droplet mismatch, but stage IIc is extended for larger droplet mismatches.

In addition to the change of stages and of their timings, wall-normal velocities strongly depend on droplet size ratio: Equal sized droplet coalescence reaches a maximum wall-normal velocity with $\bar{u}^* = 0.29$, while unequal sized droplets show decreasing maximum velocities with $\bar{u}^* = 0.18$ for $k = 0.67$ and $\bar{u}^* = 0.11$ for $k = 0.5$.

To determine the onset of free motion, the start of stage IV is defined on the basis of contact area between merged drop and solid surface; i.e., free motion starts once the contact area is zero. The

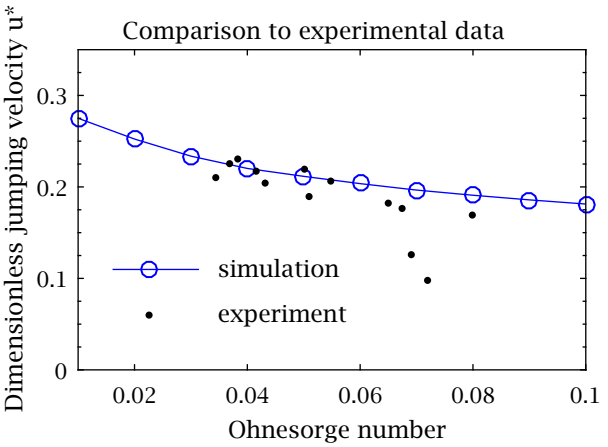

FIG. 10. Dimensionless jumping velocities as function of Ohnesorge number with contact angle $\theta = 170^\circ$ and droplet size ratio $k = 1$ from this work (o) in comparison with data from condensation experiments (•) from Enright *et al.* for the "two-camera arrangement" [18], conducted on a superhydrophobic surface.

velocity at the beginning of stage IV is called jumping velocity $\bar{u}_j^*$ in the following, as marked by crosses in Fig. 9.

B. Jumping velocity and jumping angle

Numerical simulation results of the jumping velocity in comparison to experimental results of Enright *et al.* [18] are presented in Fig. 10. The experiments were conducted on a superhydrophobic surface, where condensed droplets show nearly nonwetting behavior with small contact angle hysteresis, justifying the contact line modeling with constant contact angle in this study. The coalescing droplets were smaller than 300 μm with Bond numbers less than 0.1, allowing us to neglect the influence of gravitational forces. Because of the sensitive experimental setup, jumping velocities are subject to large fluctuations. To allow for a comparison to simulation results, only data from a "two-camera arrangement" (Figs. 6(a) and 6(c) in Enright *et al.* [18]) were selected, which show less fluctuations than the "one-camera arrangement" (Figs. 6(b) and 6(c) in Enright *et al.* [18]) used throughout most of the study. As shown in Fig. 10, simulation results with contact angle $\theta = 170^\circ$ and droplet size ratio $k = 1$ are consistent with experimentally measured jumping velocities for the band of Ohnesorge numbers investigated [18].

In Fig. 11 (left), the influence of droplet mismatch and of viscosity on jumping velocity is analyzed by variation of droplet size ratio and Ohnesorge number. Dimensionless jumping velocities are presented for droplet size ratios of $0.33 \leqslant k \leqslant 1$, Ohnesorge number within $0.001 \leqslant \mathrm{Oh} \leqslant 0.6$, and a contact angle of $\theta = 155^\circ$ and 170°.

Increasing the Ohnesorge number results in higher contribution of viscous dissipation, resulting in a damped coalescence with decreasing jumping velocities. Depending on droplet size ratio, a maximal Ohnesorge number is found under which droplet jumping occurs. For equal-sized droplets, no jumping is observed for Ohnesorge numbers with $\mathrm{Oh} > 0.5$. Other three-dimensional simulations confirm similar viscous limits [17,27]. For $\theta = 150^\circ$ and $k = 1$, there is a plateau in jumping velocity in the range $0.02 < \mathrm{Oh} < 0.06$, where both dimensionless jumping velocity and dimensionless departure time remain approximately constant (less than 5% variation). In this range, the contact area quickly decreases during the first oscillation, reducing the adhesion energy that needs to be overcome. In this manner, the effect of a decrease in jumping velocity (due to higher viscous dissipation for increasing Ohnesorge number) is outweighed by a faster decrease in adhesion energy, leading to a nearly constant jumping velocity in this range. For $\mathrm{Oh} > 0.06$, there is a transition

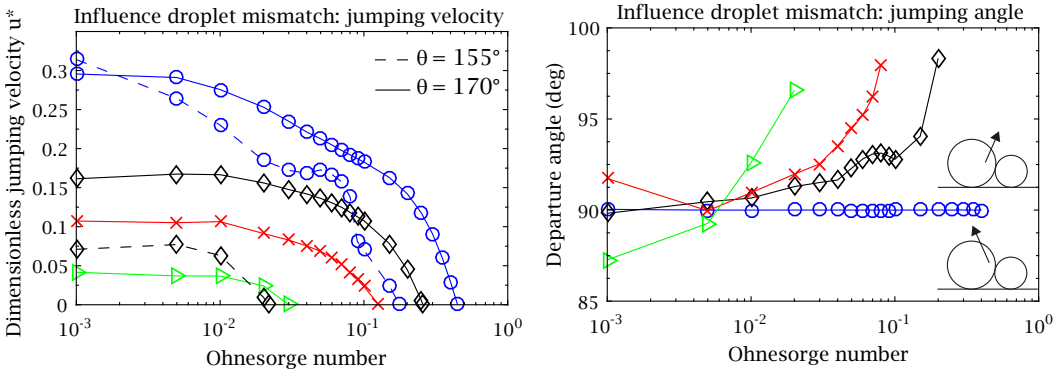

FIG. 11. Dimensionless jumping velocities (left) and departure angles with respect to the solid surface (right) as a function of Ohnesorge number for different droplet size ratios with $k = 1$ (o), $k = 0.67$ ($\diamond$), $k = 0.5$ (x), and $k = 0.33$ ($\triangleright$) for contact angle of $\theta = 155^\circ$ and $\theta = 170^\circ$.

from jumping after one oscillation to departure after two oscillations, which causes a sharp decrease in jumping velocity due to the additional viscous dissipation. For $\theta = 170^\circ$, a similar plateau as described before is not observed, since the adhesion energy plays a minor role with higher contact angles.

The jumping velocity decreases with increasing droplet mismatch; its maximum of approximately $\bar{u}_j^* = 0.3$ is observed for equal-sized droplet coalescence with $k = 1$. Similar inviscid jumping velocities of $\bar{u}_j^* = 0.28$ are reported by Enright *et al.* [18]. From Eq. (20), the jumping velocity is directly related to the conversion efficiency of the coalescence-induced droplet jumping. For equal-sized droplet jumping with contact angle $\theta = 170^\circ$, only 7% ($\bar{u}_j^* = 0.3$) of the released surface energy is convertible into translational kinetic energy, despite the absence of viscous dissipation; the remaining released energy fraction is converted into oscillatory kinetic energy. As unequal-sized droplet coalescence causes strong asymmetric flow: Oscillatory motion is enhanced while translational jumping motion is reduced. Hence, for contact angle of $\theta = 170^\circ$, the conversion efficiency drops from around 7% ($\bar{u}_j^* = 0.3$) for droplet size ratio of $k = 1$ to 2% ($\bar{u}_j^* = 0.16$) for droplet size ratio of $k = 0.67$. Similarly, the conversion efficiency for contact angle $\theta = 155^\circ$ decreases from around 7% ($\bar{u}_j^* = 0.3$) for $k = 1$ to 0.4% ($\bar{u}_j^* = 0.07$) for $k = 0.67$. Droplet adherence occurs for $k < 0.26$ ($\theta = 170^\circ$) and $k < 0.59$ ($\theta = 155^\circ$); i.e., jumping is more restricted for smaller contact angles, as expected.

While maximum jumping velocities are induced by coalescence of equal-sized droplets, jumping velocities for unequal-sized droplets decrease with droplet mismatch, as shown in Fig. 11 (left) and explained in detail in the next subsection. Because of symmetry, equal-sized droplet coalescence shows departure angles of $\theta = 90^\circ$ with respect to the solid surface, as presented in Fig. 11 (right). As unequal-sized droplet coalescence induces motion obliquely to the solid surface, jumping directions deviate from the normal direction. For Ohnesorge numbers of Oh < 0.01, unequal-sized droplets depart in the normal direction with negligible deviations of $\theta = 90 \pm 2^\circ$; for larger Ohnesorge numbers of Oh > 0.01, the deviation tends toward the s.d.s. with $\theta = 90 + 9^\circ$. The deviation grows with droplet mismatch, which is expected because of increasingly asymmetric flow. Overall, jumping direction is nearly independent of droplet mismatch, as previously shown by other authors in condensation experiments [39].

C. Transition from adhering to jumping

The static energy balance in Sec. II neglects the significant contribution of viscous dissipation and oscillatory energy. The latter has already been found for equal-size drops to have a significant influence, reducing velocity of the droplet far beyond the excess energy of droplet merging [17,18].

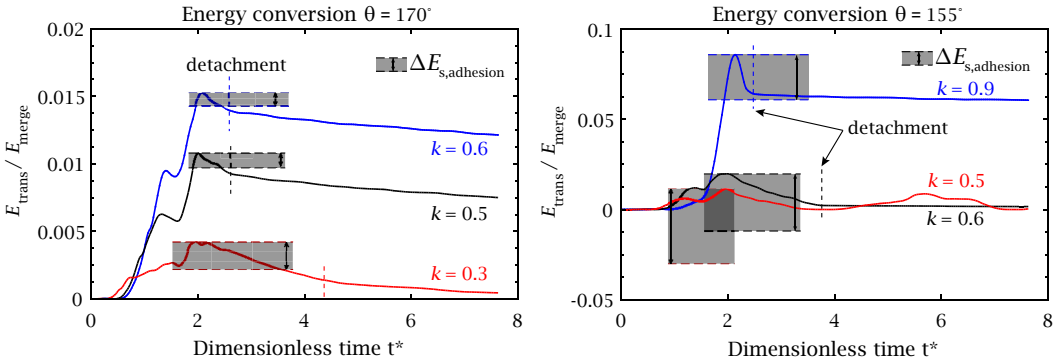

FIG. 12. Temporal evolution of the translational kinetic energy for a contact angle of $\theta = 170°$ (left) and a contact angle of $\theta = 155°$ (right) with a constant Ohnesorge number of Oh = 0.001. The gray areas indicate the energy of adhesion needed to be overcome for droplet jumping.

The importance of translational energy in the process of droplet jumping is presented in Fig. 12, illustrating its temporal evolution. The left plot presents results for a contact angle of $\theta = 170°$ and different droplet size ratios. In the course of time, the kinetic energy of the droplet increases up to its maximum value, which is prior to detachment. A rapid decrease in translational energy occurs up to the point of detachment. This decrease in translational energy is found to be similar to the adhesion energy required to be overcome for detaching a static sessile drop from the surface [Eq. (10)] and is illustrated by the gray shaded area.

The adhesion energy increases with decreasing contact angle. Thus, the relative reduction in translational kinetic energy is larger for a contact angle of $\theta = 155°$. Again, the reduction in translational energy fairly agrees with the adhesion energy. For a droplet size ratio of $k = 0.5$, the kinetic energy is not sufficient for droplet jumping, leading to an oscillation of the droplet's center of mass.

The ratio between translational and oscillatory energy depends on the droplet size ratio as presented in Fig. 13 (left). The energy ratio is plotted for the point in time of maximal translational energy. In addition, cases of droplet jumping and droplet adhesion are indicated by crosses and circles, respectively. Increasing the droplet-size mismatch tends to decrease the relative translational energy and thus the energy available to overcome the adhesion energy ($\Delta E_{\text{adhesion}}$). While the contact

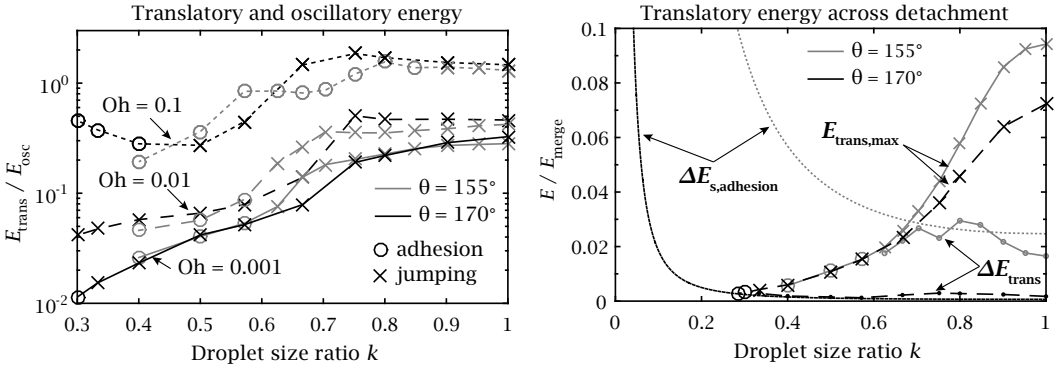

FIG. 13. Left: Ratio between translational and oscillatory energy at the point in time of maximal translational energy depending on droplet size, contact angle, and Ohesorge number. Right: Comparison between the adhesion energy of a static pending drop, the maximal translational energy, and the reduction in translational energy due to droplet detachment.

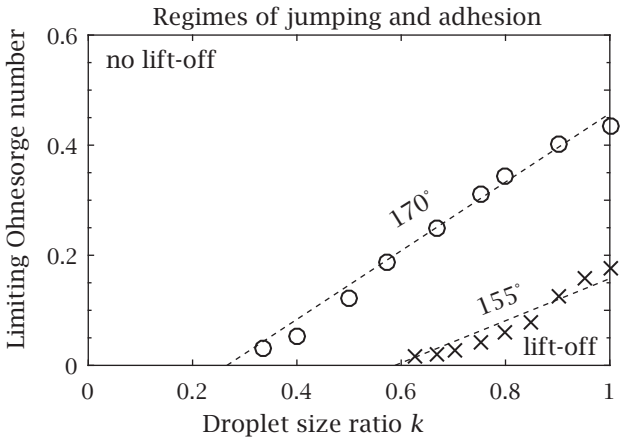

FIG. 14. Regime diagram, differentiating between lift-off and no lift-off regimes on the basis of Ohnesorge number and droplet size ratio for two wetting conditions with contact angle $\theta = 170^\circ$ and $\theta = 155^\circ$, approximated with $\mathrm{Oh} = 0.001$.

angle has only a minor influence on the energy ratio, viscous forces expressed by the Ohnesorge number affect the ratio significantly. For the inviscid limit ($\mathrm{Oh} = 0.001$), the translational energy is always far below the oscillatory energy ($\Delta E_{\mathrm{trans}}/\Delta E_{\mathrm{osc}} < 0.3$). In contrast, for the viscous case with $\mathrm{Oh} = 0.1$, the translational energy can overcome the oscillatory energy for similar droplet sizes. However, the absolute value of kinetic energy is strongly reduced due to viscous dissipation.

Figure 13 (right) shows the relation between translational energy and adhesion energy. All energies are related to the excess energy of droplet merging with the respective size ratio. Besides the adhesion energy of a static drop $E_{\mathrm{s,adhesion}}$, the maximal translational energy $E_{\mathrm{trans,max}}$ and the reduction in translational energy during the process of droplet detachment $\Delta E_{\mathrm{trans}}$ are presented. While the adhesion energy increases significantly with decreasing droplet size ratio, the maximal translational energy decreases. Both effects oppose droplet jumping. Good agreement is found between the adhesion energy of a static drop and the difference in translational energy.

The regime diagram in Fig. 14 differentiates between droplet jumping and adhesion. The limiting Ohnesorge number is shown as a function of droplet size ratio for the contact angles of $\theta = 170^\circ$ and $\theta = 155^\circ$. Of course, increasing viscous dissipation or decreasing the contact angle supports droplet adhesion. Droplet-size mismatch also opposes droplet jumping because of the reasons named in the previous paragraph.

V. CONCLUSION

In this study, the phenomenon of droplet jumping upon unequal-sized droplet coalescence was analyzed by direct numerical simulations, including a discussion on the effects of viscosity, droplet size ratios, and contact angle. For small Ohnesorge numbers, coalescence is dominated by capillary forces, inducing high jumping velocities with a maximum of $\bar{u}_{\mathrm{j}}^{*} = 0.3$. For large Ohnesorge numbers, coalescence is damped by viscous forces, restricting the jumping phenomenon to droplet coalescence with Ohnesorge number of $\mathrm{Oh} < 0.5$. Droplet size mismatch, expressed in terms of droplet size ratios, has a significant effect on the jumping velocity. Decreasing the droplet size ratio increases the ratio between adhesion forces of the merged droplet to the excess energy released due to droplet merging. In addition, the conversion in translational energy is reduced. It is shown by an evaluation of the numerical results that the change in translational energy while droplet detachment is closely related to the adhesion energy. As such, a reduced conversion rate of excess energy in translational energy obviates droplet jumping. The flow asymmetry caused by droplet mismatch limits the jumping

phenomenon: Coalescence-induced droplet jumping was observed for droplet size ratios of $k > 0.3$. This limiting condition for nearly nonwetting properties is reduced for wetting properties with stronger adhesive forces, i.e., smaller contact angles.

J.W. and P.F. contributed equally to this work.

---

[1] M. Kollera and U. Grigull, Über das Abspringen von Tropfen bei der Kondensation von Quecksilber, Wärme- Stoffübertrag. **2**, 31 (1969).

[2] J. B. Boreyko and C. H. Chen, Self-Propelled Dropwise Condensate on Superhydrophobic Surfaces, Phys. Rev. Lett. **103**, 184501 (2009).

[3] C. Lv, P. Hao, Z. Yao, Y. Song, X. Zhang, and F. He, Condensation and jumping relay of droplets on lotus leaf, Appl. Phys. Lett. **103**, 021601 (2013).

[4] X. Chen, R. S. Patel, J. A. Weibel, and S. V. Garimella, Coalescence-induced jumping of multiple condensate droplets on hierarchical superhydrophobic surfaces, Sci. Rep. **6**, 18649 (2016).

[5] A. Menchaca-Rocha, A. Martínez-Dávalos, and R. Núñez, Coalescence of liquid drops by surface tension, Phys. Rev. E **63**, 046309 (2001).

[6] N. Miljkovic, R. Enright, Y. Nam, K. Lopez, N. Dou, J. Sack, and E. N. Wang, Jumping-droplet-enhanced condensation on scalable superhydrophobic nanostructured surfaces, Nano Lett. **13**, 179 (2012).

[7] M.-K. Kim, H. Cha, P. Birbarah, S. Chavan, C. Zhong, Y. Xu, and N. Miljkovic, Enhanced jumping-droplet departure, Langmuir **31**, 13452 (2015).

[8] K. M. Wisdom, J. A. Watson, X. Qu, F. Liu, G. S. Watson, and C.-H. Chen, Self-cleaning of superhydrophobic surfaces by self-propelled jumping condensate, Proc. Natl. Acad. Sci. U.S.A. **110**, 7992 (2013).

[9] G. S. Watson, L. Schwarzkopf, B. W. Cribb, S. Myhra, M. Gellender, and J. A. Watson, Removal mechanisms of dew via self-propulsion off the gecko skin, J. R. Soc., Interface **12**, 20141396 (2015).

[10] J. B. Boreyko and C. P. Collier, Delayed frost growth on jumping-drop superhydrophobic surfaces, ACS Nano **7**, 1618 (2013).

[11] Q. Zhang, M. He, J. Chen, J. Wang, Y. Song, and L. Jiang, Anti-icing surfaces based on enhanced self-propelled jumping of condensed water microdroplets, Chem. Commun. **49**, 4516 (2013).

[12] J. B. Boreyko, Y. Zhao, and C. H. Chen, Planar jumping-drop thermal diodes, Appl. Phys. Lett. **99**, 234105 (2011).

[13] N. Miljkovic, D. J. Preston, R. Enright, and E. N. Wang, Electrostatic charging of jumping droplets, Nat. Commun. **4**, 2517 (2013).

[14] N. Miljkovic, D. J. Preston, R. Enright, and E. N. Wang, Jumping-droplet electrostatic energy harvesting, Appl. Phys. Lett. **105**, 013111 (2014).

[15] N. Miljkovic, D. J. Preston, R. Enright, and E. N. Wang, Electric-field-enhanced condensation on superhydrophobic nanostructured surfaces, ACS Nano **7**, 11043 (2013).

[16] P. Birbarah, Z. Li, A. Pauls, and N. Miljkovic, A comprehensive model of electric-field-enhanced jumping-droplet condensation on superhydrophobic surfaces, Langmuir **31**, 7885 (2015).

[17] F. Liu, G. Ghigliotti, J. J. Feng, and C.-H. Chen, Numerical simulations of self-propelled jumping upon drop coalescence on non-wetting surfaces, J. Fluid Mech. **752**, 39 (2014).

[18] R. Enright, N. Miljkovic, J. Sprittles, K. Nolan, R. Mitchell, and E. N. Wang, How coalescing droplets jump, ACS Nano **8**, 10352 (2014).

[19] J. Eggers, J. R. Lister, and H. A. Stone, Coalescence of liquid drops, J. Fluid Mech. **401**, 293 (1999).

[20] L. Duchemin, J. Eggers, and C. Josserand, Inviscid coalescence of drops, J. Fluid Mech. **487**, 167 (2003).

[21] F. Liu, G. Ghigliotti, J. J. Feng, and C.-H. Chen, Self-propelled jumping upon drop coalescence on leidenfrost surfaces, J. Fluid Mech. **752**, 22 (2014).

[22] H. Cha, C. Xu, J. Sotelo, J. M. Chun, Y. Yokoyama, R. Enright, and N. Miljkovic, Coalescence-induced nanodroplet jumping, Phys. Rev. Fluids **1**, 064102 (2016).

[23] Z. Liang and P. Keblinski, Coalescence-induced jumping of nanoscale droplets on super-hydrophobic surfaces, Appl. Phys. Lett. **107**, 143105 (2015).
[24] K. Rykaczewski, A. T. Paxson, S. Anand, X. Chen, Z. Wang, and K. K. Varanasi, Multimode multidrop serial coalescence effects during condensation on hierarchical superhydrophobic surfaces, Langmuir **29**, 881 (2013).
[25] Y. S. Nam, H. Kim, and S. Shin, Energy and hydrodynamics analyses of coalescence-induced jumping droplets, Appl. Phys. Lett. **103**, 161601 (2013).
[26] S. Farokhirad, J. F. Morris, and T. Lee, Coalescence-induced jumping of droplet: Inertia and viscosity effects, Phys. Fluids **27**, 102102 (2015).
[27] Y. Cheng, J. Xu, and Y. Sui, Numerical investigation of coalescence-induced droplet jumping on superhydrophobic surfaces for efficient dropwise condensation heat transfer, Int. J. Heat Mass Transfer **95**, 506 (2016).
[28] H. Jasak, Error analysis and estimation for the finite volume method with applications to fluid flows, Ph.D. thesis, Imperial College of Science, Technology and Medicine, London, 1996.
[29] H. Rusche, Computational fluid dynamics of dispersed two-phase flows at high phase fractions, Ph.D. thesis, Imperial College of Science, Technology and Medicine, London, 2002.
[30] C. W. Hirt and B. D. Nichols, Volume of fluid (VOF) method for the dynamics of free boundaries, J. Comput. Phys. **39**, 201 (1981).
[31] S. S. Deshpande, L. Anumolu, and M. F. Trujillo, Evaluating the performance of the two-phase flow solver interfoam, Comput. Sci. Disc. **5**, 014 (2015).
[32] P. Pischke and W. Rohlfs, Introduction and application of the smooth interface compression method in VOF (unpublished).
[33] W. Rohlfs, P. Pischke, and B. Scheid, Hydrodynamic waves in films flowing under an inclined plane, Phys. Rev. Fluids **2**, 044003 (2017).
[34] B. Lafaurie, C. Nardone, R. Scardovelli, S. Zaleski, and G. Zanetti, Modelling merging and fragmentation in multiphase flows with SURFER, J. Comput. Phys. **113**, 134 (1994).
[35] O. Basaran, Nonlinear oscillations of viscous liquid drops, J. Fluid. Mech. **241**, 169 (1992).
[36] J. E. Sprittles and Y. D. Shikhmurzaev, The dynamics of liquid drops and their interaction with solids of varying wettabilities, Phys. Fluids **24**, 082001 (2012).
[37] R. T. Eiswirth, H.-J. Bart, A. A. Ganguli, and E. Y. Kenig, Experimental and numerical investigation of binary coalescence: Liquid bridge building and internal flow fields, Phys. Fluids **24**, 062108 (2012).
[38] See Supplemental Material at http://link.aps.org/supplemental/10.1103/PhysRevFluids.2.123601 for a movie of binary droplet coalescence and subsequent self-propelled jumping.
[39] H. Cha, J. M. Chun, J. Sotelo, and N. Miljkovic, Focal plane shift imaging for the analysis of dynamic wetting processes, ACS Nano **10**, 8223 (2016).